Check for updates

Classification of zirconium-rich engineered and natural nano particles using single particle ICP-TOFMS†

Hark Karkee, Chloe Kyte and Alexander Gundlach-Graham [ID] *

Zirconium (Zr) is an important material in the field of ceramics, dentistry, and nuclear energy. It is also present in particulate form in our environment and can come from naturally occurring minerals such as zircon ($ZrSiO_4$) or from anthropogenic sources such as zirconia (ZrO_2). In this study, we present the detection and classification of Zr-particles at the individual particle level by using single-particle inductively coupled plasma time-of-flight mass spectrometry (spICP-TOFMS). Neat suspensions of engineered zirconia particles (Zr-eng) and natural zircon particles (Zr-nat) were analyzed by spICP-TOFMS, and a decision tree-based classification strategy was developed to distinguish the particle types based on their multi-elemental compositions. In both Zr-eng and Zr-nat particles, the only well-correlated element with Zr was hafnium (Hf), with Zr : Hf mass ratios converging to 47 : 1 and 75 : 1 for Zr-eng and Zr-nat, respectively. The detection of Hf along with Zr is indicative of both Zr-eng and Zr-nat particle types; however, the Zr : Hf mass ratios are too similar to be used to distinguish between individual nano- and sub-micron Zr-eng and Zr-nat particles. Instead, Zr-nat particles can be distinguished from Zr-eng particles based on the detection of minor-elements, such as iron, yttrium, lanthanum, cerium, and thorium, along with Hf in the Zr-nat particles. With our classification scheme, we demonstrate true-positive classification rates of 40% and 80% for Zr-eng and Zr-nat particle types, respectively. False-positive classification of Zr-nat as Zr-eng was below 2%. We validate our classification scheme by classifying the Zr-particles in controlled mixtures of Zr-nat and Zr-eng particles. In these mixtures, Zr-eng particles are classified at particle-number concentrations (PNCs) down to 49-times lower than that of Zr-nat particles and across a PNC range of 3 orders of magnitude.

Introduction

Zirconium (Zr) belongs to the group of naturally occurring high field strength elements (HFSEs), which also includes titanium (Ti), niobium (Nb), hafnium (Hf), and tantalum (Ta). With a crustal abundance of 0.02%, zirconium is primarily found in magmatic deposits or naturally concentrated in sedimentary deposits.[1] The major sources of Zr are minerals such as zircon ($ZrSiO_4$), baddeleyite (ZrO_2), and zirconolite ($CaZrTi_2O_7$).[2] Apart from Zr-minerals, Zr is also present as inclusions in other minerals and it is recovered as a co-product or byproduct during the processing of titanium-bearing minerals ilmenite, rutile, and leucoxene.[1,3] Commercial zirconium metal is typically extracted from zircon minerals through liquid–liquid extraction techniques.[4]

Zirconium is extensively used in the ceramic industry due to its opacity and exceptional resistance to heat, water, chemicals, and abrasion.[5] Due to its corrosion resistance and stability at high temperature (melting point = 1850 °C), zirconium is also used in nuclear applications such as in uranium nuclear fuel cladding and other reactor internal structure.[6,7] Zircon can resist various magmatic, metamorphic, and erosional processes and thus it can be used in geochronology based on the decay of U (and Th) to Pb.[8]

Zirconia (ZrO_2) particles are produced industrially by various chemical and green approaches[9,10] and have been used for applications such as catalysis[11,12] and adsorption of toxins.[10] Due to its inertness and biocompatibility,[13] nanoscale ZrO_2 has become an important ceramic material in dentistry[14,15] and bone graft applications.[16] Despite zirconia's generally recognized safety and biocompatibility, recent studies have raised concerns. Atalay *et al.* reported that 20 nm ZrO_2 particles produce apoptotic and genotoxic effects in mammalian cells.[17] Long term exposure of Zr has been reported to cause skin discoloration,[18] hypersensitivity reactions,[19] pulmonary fibrosis,[20] and/or granulomata.[21] Since zirconia particles are used for diverse applications, they inevitably find their way into environmental compartments, such as air, water, or soils. Thus, the levels of nano-zirconia in the environment should be monitored.[22,23]

Department of Chemistry, Iowa State University, Ames, Iowa, USA. E-mail: alexgg@iastate.edu

† Electronic supplementary information (ESI) available. See DOI: https://doi.org/10.1039/d4ja00094c

This journal is © The Royal Society of Chemistry 2024

J. Anal. At. Spectrom., 2024, 39, 1551–1559 | **1551**

Energy dispersive X-ray fluorescence spectroscopy is typically used for non-destructive multi-element measurement of major and minor elements in zirconium minerals; however, this technique may not be suitable for trace level-determinations.[24,25] For trace-level measurements, inductively coupled plasma (ICP) techniques such as optical emission spectrometry (ICP-OES)[26,27] and mass spectrometry (ICP-MS)[28-31] are used. ICP-MS is widely used to measure major, minor, and trace elements in zirconium crystals, for numerous applications such as high precision isotopic composition for geological exploration[30,32] and U–Pb or Th–Pb geochronology.[31,33,34] When operated in high time resolution mode, ICP-MS has also been used for single-particle (sp) analysis.[35] ICP-MS is a robust and sensitive method for single-particle measurements; however, the use of quadrupole mass analyzers that allow measurement of one (or at most two) elements or isotopes limits the application of spICP-MS for multi-element analysis.[36-38] This limitation is overcome by using a time-of-flight mass analyzer. In the past few years, inductively coupled plasma time-of-flight mass spectrometry (ICP-TOFMS) has become an instrument of choice for multi-element analysis at the single-particle or single-cell level.[39-43]

Single-particle (sp) ICP-TOFMS can be used for the quasi-simultaneous analysis of elements across the entire atomic mass range, spanning from ^6Li to ^{238}U, at high time resolution. With spICP-TOFMS, multi-elemental fingerprints of single particles or cells can be recorded.[39-41] spICP-TOFMS has been widely used for classification of natural and anthropogenic nanoparticles (NPs) and microparticles (μPs). In the past, spICP-TOFMS has been used to classify particles rich in titanium,[44-46] zinc,[47] cerium,[48-50] and platinum-group metals using classification strategies such as machine learning and decision trees.[51,52] Despite zirconium's abundance in the Earth's crust and the ubiquity of Zr particles in our environment, their classification by spICP-TOFMS remains largely unexplored.[51,53,54] Here, we report an spICP-TOFMS approach to classify zirconium-rich natural and engineered NPs and sub-micron particles at environmentally relevant concentrations and in mixtures.

Experimental section

Zircon ($ZrSiO_4$) mineral specimens were obtained from the Department of Geology and Atmospheric Sciences at Iowa State University. The zircon grains were first ground into a coarse powder using a mortar and pestle and then ball milled (SPEX mixer/mill 8000M) to achieve a fine powder. For ball milling, approximately 500 mg of zircon coarse powder was loaded into a polycarbonate grinding vial and ground for 1 hour (two sets of 30 minutes each) using methacrylate grinding balls. The fine powder obtained from ball milling was then processed using a previously established method.[45] In short, ~10 mg of fine powder was dispersed in 15 mL of ultrapure water (18.2 MΩ cm PURELAB flex, Elga LabWater, UK). The dispersed suspension was water bath sonicated (VWR Ultrasonic Cleaner, VWR, PA, USA) for 10 minutes, followed by 30 seconds of vortexing and 10 minutes of settling time. One mL of the supernatant was diluted with ultrapure water and used as an intermediate stock suspension of $ZrSiO_4$ NPs for spICP-TOFMS measurements. Initial spICP-

measurements of the diluted intermediate stock suspension were done to determine the particle number concentrations (PNCs).

Zirconium dioxide (ZrO_2) powder was purchased from Sigma-Aldrich (St. Louis MO, USA) and used as a source of zirconium engineered particles (i.e. Zr-eng). A neat suspension of ZrO_2 was prepared by dispersing approximately 2 mg of the ZrO_2 powder into 1.5 mL ultrapure water in a 2 mL centrifuge tube. This was followed by 30 seconds of vortexing and 60 seconds of ultrasonication using a VialTweeter (Hielscher UP200st, Germany, 100 W, cycle of 10 seconds on and 5 seconds off). The sample was then centrifuged for two minutes at 4000 rpm using Mini centrifuge (Costar, USA). The estimated size cutoff from this centrifugation was around 300 nm based on Stoke's law and particle density of 5.9 g cm^{-3}. 900 μL of supernatant suspension was transferred to a new 4 mL vial and used for further spICP-TOFMS measurements. Initial spICP-TOFMS measurements of the diluted intermediate stock suspension were done to determine the PNCs.

Mixtures of Zr-nat and Zr-eng particles were prepared by spiking Zr-eng particles into a stock suspension of Zr-nat particles and vice versa. In the first mixed suspension, a Zr-eng particle suspension (PNC ≈ 250 000 mL^{-1}) was spiked into a Zr-nat suspension (PNC ≈ 75 000 particles per mL). This mixed-particle stock suspension was then serially diluted with the background Zr-nat suspension as the diluent to obtain suspensions with Zr-eng PNCs across three orders of magnitude. In the second mixed-particle suspension, a Zr-nat particle suspension (PNC ≈ 250 000 mL^{-1}) was spiked into a background Zr-eng particle suspension (PNC ≈ 37 000 mL^{-1}). This mixed-particle stock suspension was then serially diluted with the background Zr-eng suspension as the diluent to obtain suspensions with Zr-nat PNCs across three orders of magnitude.

Preparation of calibration solutions

Single-element standards (High-Purity Standards, SC, USA) were used to prepare two different multi-element calibration solutions. Dilutions were performed gravimetrically (ML204T/A00, Mettler-Toledo, Switzerland). The first multi-element calibration solution consisted of Mg, Al, Mn, Fe, Y, Cs, La, Ce, Pb, Th and U diluted in 2% sub-boiled trace metal grade nitric acid (Fisher Scientific, Fair Lawn, NJ, USA). Ultra-trace sub-boiled concentrated HNO_3 was distilled in-house (DST-1000, Savillex Corp., MN, USA). The second multi-element calibration solution consisted of Ti, Zr, Nb, Ho, Hf, Ta and Bi diluted in 2% HNO_3 + 0.1% HF (Fisher Scientific, Fair Lawn, NJ, USA). The range of element concentrations in the calibration solutions was from 0 ng mL^{-1} to 500 ng mL^{-1}. Single-element solutions of Au with concentrations from 0 ng mL^{-1} to 500 ng mL^{-1} were prepared in 2% (v/v) HCl (TraceSelect grade, Honeywell-Fluka, Charlotte, NC, USA) and used to calibrate the transport efficiency into the plasma with the particle-size method.[55]

spICP-TOFMS measurements and data processing

An icpTOF-S2 instrument (TOFWERK AG, Thun, Switzerland) was used for all measurements. Detailed instrument operation parameters are provided in Table S1.† ToFDAQ Recorder

1552 | J. Anal. At. Spectrom., 2024, 39, 1551–1559

This journal is © The Royal Society of Chemistry 2024

(TOFWERK AG, Thun, Switzerland) was used to collect all the ICP-TOFMS data and "TOF Single-Particle Investigator" (TOF-SPI) was used for data processing.[56] TOF-SPI is a batch analysis program written in a LabVIEW (LabVIEW 2018, National Instruments Corp., TX, USA) and used to calculate element background signals and single-particle critical values ($L_{c,sp}$), determine absolute element sensitivities (TofCts g^{-1}), background subtract data, correct split-particle events,[57] quantify element masses in single particles, and determine PNCs. Single-particle critical values ($L_{c,sp,i}$ values) are detection thresholds for each element, i, used to separate particle derived signals from a steady state background signals.[58,59] $L_{C,sp,i}$ values can be converted to critical mass values ($X_{C,sp,i}^{mass}$) based on absolute sensitivities for each element, i. In Table S2,† we provide the nuclides used for quantification of elements with typical absolute sensitivities and critical mass values.

The particle-size method was used to calculate element mass amounts per particle and determine PNCs.[55] Briefly, ultra-uniform 50 nm diameter gold NPs (nanoComposix, now Fortis Life Sciences, San Diego, USA) were measured by spICP-TOFMS and used to determine the absolute sensitivity for gold (TofCts g^{-1}). Standard solutions of Au prepared were then used to determine the relative sensitivity of Au (TofCts s^{-1}/g mL^{-1}). The ratio of the relative sensitivity to absolute sensitivity of Au was used to calculate plasma-uptake rate (q_{plasma}, mL s^{-1}). The ratio for q_{plasma} to nebulizer uptake rate (q_{neb}) was used to determine nebulization transport efficiency (η_{neb}, %). To obtain absolute sensitivities of analyte elements, relative sensitivities of each element from solution calibration curves were divided by q_{plasma}. All calibration calculations were performed in TOF-SPI.

Particle derived classification of Zr-particles as either natural zircon particles (Zr-nat), engineered zirconia particles (Zr-eng), or unclassified single-metal (sm) zirconium-containing particles (unc. smZr) was performed using a custom written Streamlit webapp (version 1.23.1) based on Python language (version 3.11.4) using PyCharm (Community Edition 2023.1.2) as an integrated development environment (IED). The source codes for the classification app are available on GitHub (https://github.com/TOFMS-GG-Group). Details of the classification scheme are provided below.

Throughout this manuscript, we refer to detected particle signals as "NPs"; in fact, we detect both nano- (diameter < 100 nm) and micro-particles (diameter > 0.1 μm). With spICP-TOFMS, some elements commonly present NPs, such as carbon, nitrogen, oxygen, sulfur, and fluorine, are not readily detectable at the single-particle level. In the case of zircons (ZrSiO$_4$), the measurement of silicon at the single-particle level was also not possible because of the high background of N$_2^+$ in the ICP and low sensitivity for ^{28}Si$^+$. We use the terms "single-metal" and "multi-metal" NPs (sm-NP and mm-NP) to refer to measured particle events with either one or with two or more ICP-TOFMS-detectable elements, respectively.

Results and discussion

Characterization of Zr-NPs

To determine the multi-element compositions of the Zr-nat and Zr-eng NP types, we first analyzed neat suspensions of these NPs by spICP-TOFMS. In Fig. 1, we plot the unique elemental fingerprints of Zr-eng and Zr-nat NPs as heat maps. In these maps, the mass amounts of each element in all measured NPs are shown on a false color scale. From the heat maps in Fig. 1, it is clear that the Zr-nat and Zr-eng NPs have different spICP-TOFMS measurable multi-element fingerprints: while Zr and Hf are the only measurable elements in the Zr-eng NPs, the Zr-nat NPs also contain significant amounts of other elements, including, Fe, Y, La, Ce, and Th. According to spICP-TOFMS measurements and quantification with 100% oxide normalization, the Zr-eng NPs contain – on average – 98.5% ZrO$_2$ and 1.5% HfO$_2$ by mass. This is in agreement with the manufacture's label, which states that the Zr-eng NPs contain ~2.0% of HfO$_2$ as an impurity. In Fig. 1c, we plot a histogram of the equivalent spherical diameters of the Zr-eng particles, as measured by spICP-TOFMS. To estimate the diameter, we converted measured Zr mass to mass of ZrO$_2$, and assumed that the NPs are spherical with a density of 5.89 g cm^{-3}. Based on three replicates, the average NP size of the Zr-eng particles was 62.7 ± 0.9 nm (±1 standard deviation). In all replicates, 95% of the particles had an estimated diameter less than 100 nm. Approximately 60% of the Zr-eng NPs are measured as single-element Zr NPs (i.e. as sm-Zr NPs). As shown in Fig. S1,† sm-Zr NPs are recorded predominantly as smaller NPs, with >95% of sm-Zr NPs having a Zr mass <1 fg (ZrO$_2$ diameter = 76 nm). Because Hf is a minor component of the Zr-eng NPs, it is only measurable in larger NPs. If the size distribution of Zr-eng NPs was larger or the critical mass of Hf was significantly lower, then Hf would be recorded in a larger fraction of events from Zr-eng NPs.

Unlike Zr-eng NPs, the element signatures recorded by spICP-TOFMS for Zr-nat NPs consist of a host of elements including Al, Ti, Fe, Y, Zr, La, Ce, Ho, Hf, Pb, Th, and U, as shown in the heat map in Fig. 1b. According to spICP-TOFMS measurements, Zr and Fe are the major elements, with Zr and Fe accounting for 73 ± 2% and 18 ± 2% of the total measured mass per NP, respectively. The Zr-nat NPs had minor mass fractions of Th (3.4 ± 0.1%), Al (3.1 ± 0.3%), Y (0.8 ± 0.4%) and Hf (0.78 ± 0.02%). Our measurement of Hf mass fraction aligns with previously reported values (0.5–2.0%) for Hf content in Zr minerals.[4] All other elements are present in trace amounts. We report detailed mass fraction data of all elements in Zr-nat NPs in Table S3.† In Fig. 1d, we plot a histogram of the equivalent spherical diameters of the Zr-nat NPs, as measured by spICP-TOFMS. The estimated diameters were determined exclusively based on the measured mass of Zr, which was converted to mass of ZrSiO$_4$ based on known mineral stoichiometry. We further assumed that the NPs were spherical with a density of 4.7 g cm^{-3}. The average diameter of the Zr-nat NPs was 85 ± 1 nm (standard deviation of three replicates). Approximately 70% of all measured Zr-nat NPs had an equivalent spherical diameter less than 100 nm. Approximately 18% of measured Zr-nat NPs were recorded with a sm-Zr signature; like the Zr-eng NPs, the particle events with a sm-Zr signature contained less Zr mass (see Fig. S1†).

Despite the association of Zr with multiple elements in Zr-nat NPs, the only element correlated with Zr is Hf. In Fig. S2,† we present the correlation matrix of all elements quantified in the Zr-nat NPs. In the Zr-nat particles, some elements, such as

This journal is © The Royal Society of Chemistry 2024

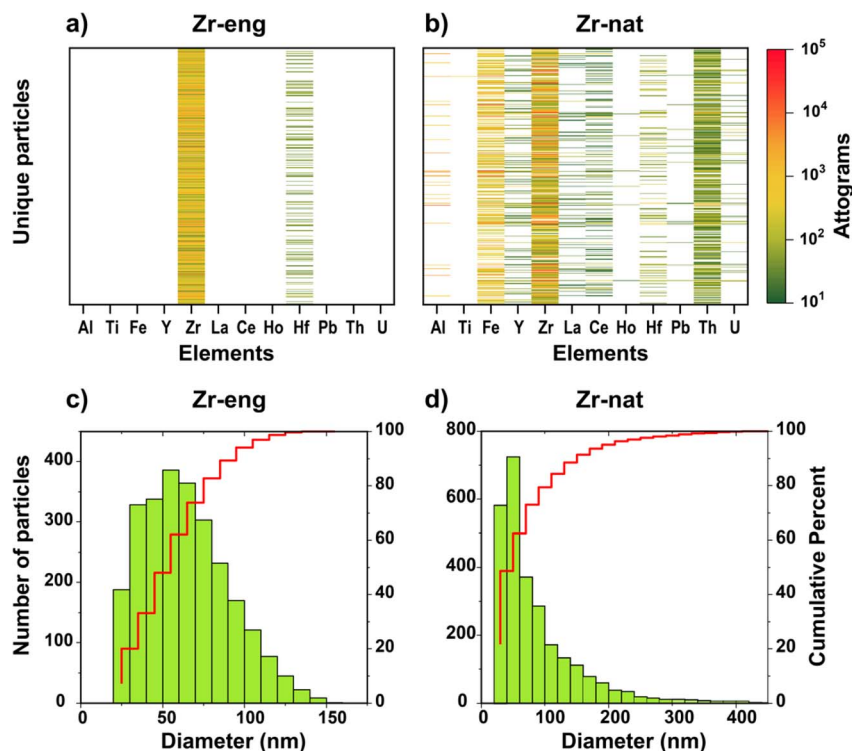J. Anal. At. Spectrom., 2024, **39**, 1551–1559 | **1553**

Fig. 1 (a and b) Heat maps showing the elemental composition of Zr-eng NPs and Zr-nat NPs. (c and d) Histograms of the measured equivalent spherical diameters of Zr-eng and Zr-nat NPs. Particle diameters were estimated assuming spherical shape and are based on measured Zr mass, known stoichiometry of the minerals, and known densities. Heat maps and histograms are plotted using the data from single measurement.

Ce and La, are well correlated with each other, but not with Zr or Hf. This correlation is expected because the similar chemistries of these elements cause them to be present at conserved ratios when detected. However, as minor or trace elements, these elements do not substitute for Zr or Hf in the crystal lattice and so aren't correlated with Zr or Hf. Zr and Hf are also correlated in Zr-eng NPs. In Fig. 2, we plot the mass ratios of Zr : Hf as a function of Zr mass for both the Zr-eng and Zr-nat NPs. The mass ratio of Zr : Hf converges to 47 : 1 and 75 : 1 in Zr-eng and Zr-nat NPs, respectively. In Fig. 2, we plot the 95% confidence

bands predicted by Poisson statistics for the experimental mass ratio as determined by Monte Carlo simulation. As seen, the determined mass ratios for the Zr-eng NPs fit well within the expected Poisson confidence bands; however, the Zr : Hf ratio from the Zr-nat NPs is more disperse than predicted by Poisson statistics: this dispersion is likely caused by true mass fraction variation of Zr and Hf in the Zr-nat NPs. The dispersion in the Zr : Hf mass ratio may be attributed to compositional variations in Zr and Hf during magmatic and metamorphic crystallization processes. Such variations result in the formation of zones
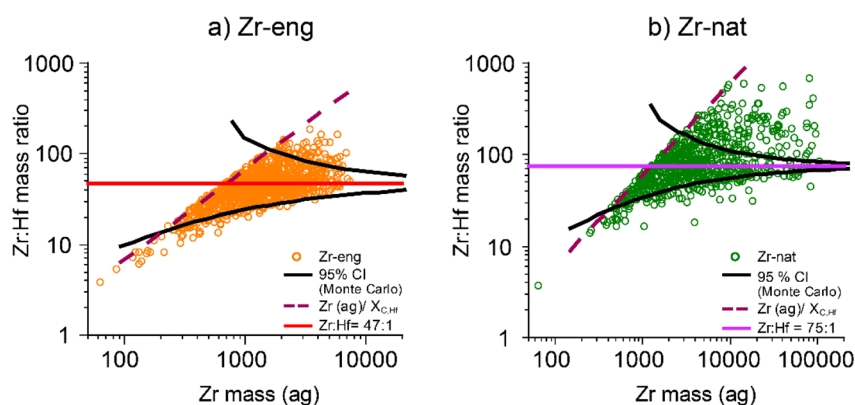

Fig. 2 Mass ratio of Zr : Hf plotted against Zr mass in multi-element ZrHf particles of Zr-eng (a) and Zr-nat (b). The Zr : Hf mass ratios converge to 47 and 75 in the Zr-eng and Zr-nat NPs, respectively. The ratios follow an estimated Monte-Carlo error, however, there is some dispersion in higher mass ratios. The black confidence bands are determined at the 95% confidence level and a known, true, Zr : Hf mass ratio.

within zircons, exhibiting diverse compositions of Zr and Hf, as well as other elements such as Si, P, Y, rare earth elements (REE), uranium (U), and thorium (Th), with variations of up to an order of magnitude.[8,60] For both Zr-eng and Zr-nat NPs, the minimum measured Zr : Hf mass ratio does not go below 3 : 1. However, the maximum measured mass ratio of Zr : Hf is quite different between the NP types: 200 : 1 for Zr-eng NPs and 700 : 1 for Zr-nat NPs.

Classification scheme and its accuracy

To distinguish between Zr-eng and Zr-nat NPs at the single-particle level, there must be differences in either multi-element presence or elemental ratios between the two NP types. As seen in Fig. 2, while the average ratio of Zr : Hf in the Zr-eng and Zr-nat NPs are different, the majority of NPs do not have measurable differences in Zr : Hf. Likewise, because the sm-Zr element signature is recorded for both Zr-eng and Zr-nat NPs and these NPs have similar mass amounts of Zr (see Fig. S1†), events with sm-Zr signatures cannot be distinguished as Zr-eng or Zr-nat. The most prominent distinguishing characteristic between multi-element signatures recorded for the Zr-eng and Zr-nat is the detection of associated elements other than Hf in the Zr-nat NPs. In the spICP-TOFMS data of Zr-nat NPs, more than 80% of NPs with a measurable amount Zr also have a measurable amount of another element. Moreover, up to 98% of the NPs with mm-Zr recorded signatures include detection of an element or elements other than Hf. Because the mass fraction of Hf in Zr-nat NPs is ~75 : 1, Hf is present at a mass amount below the critical mass of the spICP-TOFMS measurement in a majority of Zr-nat NPs. The most common element associations with Zr in the Zr-nat NPs are Fe, Th, and Ce (see Fig. S3†). These elements do not have a conserved mass ratio with Zr in the Zr-nat NPs; however, the detection of these elements does indicate that the Zr-rich NP is not Zr-eng, and so can be classified as Zr-nat.

In Fig. 3, we present our decision tree for the classification of Zr-rich NPs as Zr-eng, Zr-nat, and unclassified (unc.) sm-Zr NPs. In this decision tree, we classify NPs with a Zr–Hf mm-NP signature as Zr-eng, NPs with a Zr–Hf–X or Zr–X signature (where X is Fe, La, Ce, Pb, Th, or U) as Zr-nat, and all NPs with a sm-Zr signature as unc. sm-Zr. We included the unc. sm-Zr
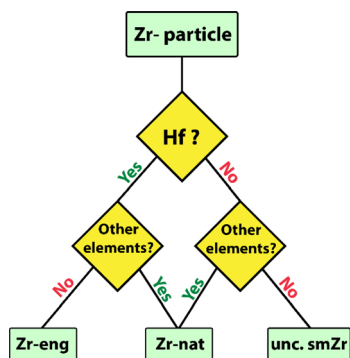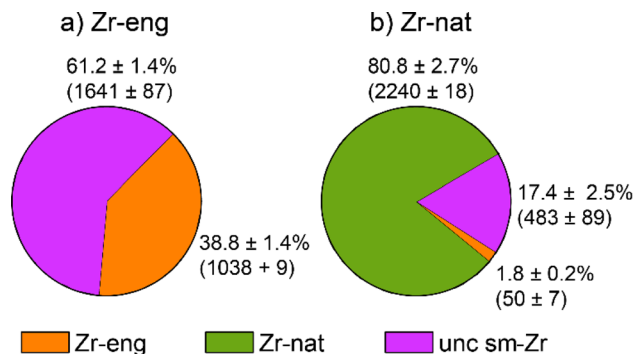

Fig. 4 Pie charts showing classification accuracy of Zr-eng (a) and Zr-nat (b) particles. The classification percentage (and numbers in parentheses) are based on average values from triplicate measurements with their associated standard deviations.

category because a large number of NPs with a sm-Zr signature are detected from both Zr-eng and Zr-nat NPs, and so these smZr NPs cannot be definitively classified. In Fig. 4, we present pie charts showing classification accuracy of each of the NP types from neat suspensions of Zr-eng and Zr-nat NPs. Error is presented as the standard deviation of three replicate spICP-TOFMS measurements. As seen, our classification scheme enables true-positive classification of ~40% of the Zr-eng NPs and ~80% of the Zr-nat NPs. The classification scheme minimizes false-positive classification: 0% of Zr-eng NPs are falsely classified as Zr-nat and ~2% of Zr-nat NPs are falsely classified as Zr-eng. Our classification approach allows for many false negatives with ~60% of Zr-eng and ~20% of Zr-nat NPs classified as "unclassifiable." This unclassifiable category is included because of the large analytical uncertainty for the measurement of secondary elements in small NPs. Thus, the false negative classifications will change as a function of particle-size distribution (PSD); spICP-TOFMS analysis of NPs with a larger median particle size would result in fewer false negatives. By minimizing false-positive classifications (at the expense of having more false-negatives), classification of NPs in variable number concentrations is possible. For example, Zr-eng NPs in a large background of Zr-nat NPs is only possible with a low false-positive rate from the Zr-nat NPs.

Quantitative analysis of Zr-eng and Zr-nat particles

Engineered NPs (ENPs) in the environmental samples are often present at low PNCs compared to the particles of natural origin.[61] This makes the accurate quantification of ENPs a difficult task, especially when the engineered and natural particles have similar elemental compositions.[45,49] Here, we test our classification scheme of Zr-NPs, by mixing Zr-eng and Zr-nat NPs at different PNCs, measuring the NP mixtures with spICP-TOFMS, and then classifying the NPs. We provide results of our determined number concentrations of each NP type (i.e. Zr-eng or Zr-nat) in these mixtures in Fig. 5. In Fig. 5a, we present results for a mixture with increasing Zr-eng PNC and a constant background of Zr-nat particles. Our results show that Zr-eng NPs can be classified across three orders of magnitude with
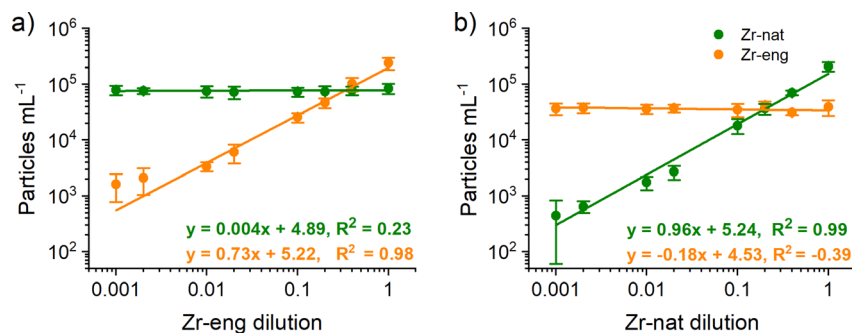

Fig. 3 Decision tree for the classification of Zr-eng and Zr-nat NPs.

This journal is © The Royal Society of Chemistry 2024

J. Anal. At. Spectrom., 2024, **39**, 1551–1559 | **1555**

Fig. 5 (a) Quantitative analysis of Zr–eng NPs spiked into a suspension of Zr–nat NPs. Based on serial dilution of the spiked suspension with a solution containing a constant PNC of Zr–nat NPs, we expect the slope of the determined Zr–eng PNC *vs.* dilution to be equal to 1 and Zr–nat PNC *vs.* dilution to be constant. (b) Quantitative analysis of Zr–nat NPs spiked a various number concentrations (*i.e.* dilution amounts) into a suspension with a constant number concentration of Zr–nat NPs. The average PNCs with associated standard deviation are based on triplicate measurements.

PNC ratios of Zr–eng : Zr–nat that range from 1 : 49 to 2.8 : 1. In Fig. 5a, the slope of 0.73 on the log–log plot of Zr–eng PNC to Zr–eng dilution indicates the influence of false-positive classification of Zr–nat NPs. Based on our analysis of neat Zr–nat suspensions, the false-positive rate from the Zr–nat NPs is ~2%. This indicates that Zr–eng : Zr–nat ratio of ~1 : 50 would produce around a 50% over-estimation in the Zr–eng PNC false positive classification rate of Zr–nat NPs. We observe this in Fig. 5a, where the measure a lowest number concentration ratio of 1 : 49, even when the theoretical PNC ratio goes down to ~1 : 300. The small number of false positive Zr–eng classifications from the background Zr–nat particles limits the lower floor of the dynamic range of Zr–eng that can be accurately classified.

In Fig. 5b, we present results from spICP-TOFMS analysis of mixtures with increasing Zr–nat PNC and a stable Zr–eng NP background. As seen, because Zr–eng NPs do not produce false positives, detection of low PNCs of Zr–nat particles is not interfered, and the slope of the curve is ~1. The detected particle number ratios of Zr–eng : Zr–nat ranged from 83 : 1 to 1 : 5, which spans 3 orders of magnitude. Additionally, we observe that the influence of false-positive Zr–eng classification from the Zr–nat NPs onto the constant background of Zr–eng particles is minimal. Though the spiked Zr–nat particles produce false positive Zr–eng classifications, the number of these false positives is small compared to the number of background Zr–eng particles. A slope near zero for Zr–eng PNC *vs.* Zr–nat dilution amount demonstrates no influence in Zr–eng PNC due to spiked Zr–nat across three orders of magnitude.

measurements, the true-positive classification rate for the Zr–eng NPs was ~40% and the false-positive rate was zero. Zr–nat NPs are classified based on the association of Zr with any other element, regardless of the presence or absence of Hf. In our measurements, the true-positive rate for Zr–nat NPs was ~80% and ~2% of Zr–nat produced false-positive Zr–eng classification. We validated our classification strategy by classifying Zr–eng and Zr–nat NPs in mixtures across three orders of magnitude. We demonstrated that Zr–eng NPs can be measured at number concentrations 49-times lower than that of Zr–nat particles.

All the experiments in this work were done on neat suspensions and mixtures of known Zr–nat and Zr–eng NPs. This experimental design was used to build and validate our particle classification scheme. Our spICP-TOFMS classification scheme for Zr-rich particles supports other classification schemes already developed for the classification of Ti-rich[45] and Ce-rich[49] particle types. In the future, this work will be expanded to include the analysis of more diverse Zr–nat and Zr–eng NP types in order to investigate the robustness of the methodology for more complex NP mixtures. Likewise, the work will be extended to characterize and quantify Zr–nat and Zr–eng in more complex environmental samples such as river water, soil, and urban runoff.

Conflicts of interest

The authors do not have any conflicts of interest to declare.

Conclusion

We reported the classification of zirconium NPs of natural origin (zircon or Zr–nat) and anthropogenic origin (zirconia or Zr–eng) at individual particle level using single-particle ICP-TOFMS. We characterized both natural and anthropogenic NPs in detail and developed a classification scheme based on the unique elemental compositions measured in these particle types. Zr–eng NPs are classified based on the association of Zr with Hf in the absence of any other element. In our

Acknowledgements

1556 | *J. Anal. At. Spectrom.*, 2024, **39**, 1551–1559

This journal is © The Royal Society of Chemistry 2024

References

1 C. Perks and G. Mudd, Titanium, zirconium resources and production: A state of the art literature review, *Ore Geol. Rev.*, 2019, **107**, 629–646.

2 R. H. Nielsen, J. H. Schlewitz, H. Nielsen and U. Staff, Zirconium and zirconium compounds, *Kirk-Othmer Encycl. Chem. Technol.*, 2000, 1–46.

3 A. R. Milnes and R. W. Fitzpatrick, Titanium and Zirconium Minerals, in *Minerals in Soil Environments*, 2018, pp. 1131–1205.

4 S. K. Dutta and D. R. Lodhari, Zirconium, in *Extraction of Nuclear and Non-ferrous Metals*, 2018, pp. 53–61.

5 E. Snyders, J. H. Potgieter and J. T. Nel, The upgrading of an inferior grade zircon to superior opacifier for sanitary ware and glazes, *J. South. Afr. Inst. Min. Metall.*, 2005, **105**(7), 459–463.

6 L. Xu, Y. Xiao, A. van Sandwijk, Q. Xu and Y. Yang, Production of nuclear grade zirconium: A review, *J. Nucl. Mater.*, 2015, **466**, 21–28.

7 H. G. Rickover, L. D. Geiger and B. Lustman, History of the development of zirconium alloys for use in nuclear reactors, *Energy Research and Development Administration*, Div. of Naval Reactors, Washington, DC (USA), 1975.

8 F. Corfu, J. M. Hanchar, P. W. O. Hoskin and P. Kinny, Atlas of Zircon Textures, *Rev. Mineral. Geochem.*, 2003, **53**(1), 469–500.

9 N. Kumari, S. Sareen, M. Verma, S. Sharma, A. Sharma, H. S. Sohal, S. K. Mehta, J. Park and V. Mutreja, Zirconia-based nanomaterials: recent developments in synthesis and applications, *Nanoscale Adv.*, 2022, **4**(20), 4210–4236.

10 B. Debnath, M. Majumdar, M. Bhowmik, K. L. Bhowmik, A. Debnath and D. N. Roy, The effective adsorption of tetracycline onto zirconia nanoparticles synthesized by novel microbial green technology, *J. Environ. Manage.*, 2020, **261**, 110235.

11 F. Qiu, Y. Li, D. Yang, X. Li and P. Sun, Heterogeneous solid base nanocatalyst: preparation, characterization and application in biodiesel production, *Bioresour. Technol.*, 2011, **102**(5), 4150–4156.

12 F. Zhou, N. Lu, B. Fan, H. Wang and R. Li, Zirconium-containing UiO-66 as an efficient and reusable catalyst for transesterification of triglyceride with methanol, *J. Energy Chem.*, 2016, **25**(5), 874–879.

13 O. Roualdes, M. E. Duclos, D. Gutknecht, L. Frappart, J. Chevalier and D. J. Hartmann, In vitro and in vivo evaluation of an alumina-zirconia composite for arthroplasty applications, *Biomaterials*, 2010, **31**(8), 2043–2054.

14 M. M. Gad, R. Abualsaud, A. Rahoma, A. M. Al-Thobity, K. S. Al-Abidi and S. Akhtar, Effect of zirconium oxide nanoparticles addition on the optical and tensile properties of polymethyl methacrylate denture base material, *Int. J. Nanomed.*, 2018, **13**, 283–292.

15 U. Lohbauer, A. Wagner, R. Belli, C. Stoetzel, A. Hilpert, H. D. Kurland, J. Grabow and F. A. Muller, Zirconia nanoparticles prepared by laser vaporization as fillers for dental adhesives, *Acta Biomater.*, 2010, **6**(12), 4539–4546.

16 X. He, Y. Z. Zhang, J. P. Mansell and B. Su, Zirconia toughened alumina ceramic foams for potential bone graft applications: fabrication, bioactivation, and cellular responses, *J. Mater. Sci.: Mater. Med.*, 2008, **19**(7), 2743–2749.

17 H. Atalay, K. A. Celi and F. Ayaz, Investigation of genotoxic and apoptotic effects of zirconium oxide nanoparticles (20 nm) on L929 mouse fibroblast cell line, *Chem.-Biol. Interact.*, 2018, **296**, 98–104.

18 H. J. Ryu, S. J. Yoon, J.-T. Park, Y. H. Kim, J. M. Jung, M.-H. Park, I. J. Rhyu and D.-Y. Kwon, Skin discolouration with acute onset parkinsonism secondary to systemic zirconium intoxication, *Ann. Clin. Biochem.*, 2014, **51**(1), 97–100.

19 T. Tuomi, Hypersensitivity Pneumonitis and Exposure to Zirconium Silicate in a Young Ceramic nle Worker, *Am. Rev. Respir. Dis.*, 1993, **148**, 1089–1092.

20 T. Bartter, R. S. Irwin, J. L. Abraham, A. Dascal, G. Nash, J. S. Himmelstein and P. J. Jederlinic, Zirconium compound-induced pulmonary fibrosis, *Arch. Intern. Med.*, 1991, **151**(6), 1197–1201.

21 P. J. Lopresti and G. W. Hambrick, Zirconium granuloma following treatment of rhus dermatitis, *Arch. Dermatol.*, 1965, **92**(2), 188–191.

22 D. Meza-Figueroa, M. Pedroza-Montero, M. Barboza-Flores, S. Navarro-Espinoza, R. Ruiz-Torres, A. Robles-Morua, F. Romero, B. Schiavo, B. Gonzalez-Grijalva, M. Acosta-Elias and A. Mendoza-Cordova, Identification of refractory zirconia from catalytic converters in dust: An emerging pollutant in urban environments, *Sci. Total Environ.*, 2021, **760**, 143384.

23 N. Hichem, Z. Hadjer, S. Fateh, L. Feriel and Z. Wang, The potential exposure and hazards of zirconia nanoparticles: A review, *Ecotoxicology and Environmental Contamination*, 2022, **17**(1), 1–21.

24 S. Jayabun and A. Sengupta, Development of Methodologies for the Chemical Quality Control of Zircon, A Precursor for Zirconium Production, *ChemistrySelect*, 2021, **6**(3), 376–388.

25 A. Sengupta, S. Thulasidas and V. Natarajan, Trace level determination of precious metals in aqueous medium, U, Th and Zr based nuclear materials by ICP-AES and EDXRF: a comparative study, *J. Radioanal. Nucl. Chem.*, 2015, **303**, 2421–2429.

26 M. Banno, E. Tamiya and Y. Takamura, Determination of trace amounts of sodium and lithium in zirconium dioxide (ZrO_2) using liquid electrode plasma optical emission spectrometry, *Anal. Chim. Acta*, 2009, **634**(2), 153–157.

27 S. Shariati and Y. Yamini, Cloud point extraction and simultaneous determination of zirconium and hafnium using ICP-OES, *J. Colloid Interface Sci.*, 2006, **298**(1), 419–425.

28 Q. Xie and R. Kerrich, Optimization of operating conditions for improved precision of zirconium and hafnium isotope ratio measurement by inductively coupled plasma mass spectrometry (ICP-MS), *J. Anal. At. Spectrom.*, 1995, **10**(2), 99–103.

This journal is © The Royal Society of Chemistry 2024

J. Anal. At. Spectrom., 2024, **39**, 1551–1559 | **1557**

29 J. He, J. Meija and L. Yang, Determination of the Isotopic Composition of Zirconium Using MC-ICPMS and a Regression Model for Mass Bias Correction, *Anal. Chem.*, 2021, **93**(12), 5107–5113.

30 M. Schönbächler, M. Rehkämper, D.-C. Lee and A. N. Halliday, Ion exchange chromatography and high precision isotopic measurements of zirconium by MC-ICP-MS, *The Analyst*, 2004, **129**(1), 32–37.

31 B. Shaulis, T. J. Lapen and A. Toms, Signal linearity of an extended range pulse counting detector: Applications to accurate and precise U-Pb dating of zircon by laser ablation quadrupole ICP-MS, *Geochem., Geophys., Geosyst.*, 2010, **11**(11), DOI: 10.1029/2010GC003198.

32 H. G. D. Tompkins, L. J. Zieman, M. Ibañez-Mejia and F. L. H. Tissot, Zirconium stable isotope analysis of zircon by MC-ICP-MS: methods and application to evaluating intra-crystalline zonation in a zircon megacryst, *J. Anal. At. Spectrom.*, 2020, **35**(6), 1167–1186.

33 Z. Chang, J. D. Vervoort, W. C. McClelland and C. Knaack, U-Pb dating of zircon by LA-ICP-MS, *Geochem., Geophys., Geosyst.*, 2006, 7(5), DOI: 10.1029/2005GC001100.

34 M. Guillong, J. T. Sliwinski, A. Schmitt, F. Forni and O. Bachmann, U-Th Zircon Dating by Laser Ablation Single Collector Inductively Coupled Plasma-Mass Spectrometry (LA-ICP-MS), *Geostand. Geoanal. Res.*, 2016, **40**(3), 377–387.

35 C. Degueldre, P. Y. Favarger and C. Bitea, Zirconia colloid analysis by single particle inductively coupled plasma–mass spectrometry, *Anal. Chim. Acta*, 2004, **518**(1–2), 137–142.

36 M. D. Montaño, H. R. Badiei, S. Bazargan and J. F. Ranville, Improvements in the detection and characterization of engineered nanoparticles using spICP-MS with microsecond dwell times, *Environ. Sci.: Nano*, 2014, **1**(4), 338–346.

37 J. W. Olesik and P. J. Gray, Considerations for measurement of individual nanoparticles or microparticles by ICP-MS: determination of the number of particles and the analyte mass in each particle, *J. Anal. At. Spectrom.*, 2012, **27**(7), 1143–1155.

38 K. Ding, S. Liang, C. Xie, Q. Wan, C. Jin, S. Wang, Y. T. Tang, M. Zhang and R. Qiu, Discrimination and Quantification of Soil Nanoparticles by Dual-Analyte Single Particle ICP-QMS, *Anal. Chem.*, 2022, **94**(30), 10745–10753.

39 O. Borovinskaya, S. Gschwind, B. Hattendorf, M. Tanner and D. Gunther, Simultaneous mass quantification of nanoparticles of different composition in a mixture by microdroplet generator-ICPTOFMS, *Anal. Chem.*, 2014, **86**(16), 8142–8148.

40 O. Borovinskaya, B. Hattendorf, M. Tanner, S. Gschwind and D. Günther, A prototype of a new inductively coupled plasma time-of-flight mass spectrometer providing temporally resolved, multi-element detection of short signals generated by single particles and droplets, *J. Anal. At. Spectrom.*, 2013, **28**(2), 226–233.

41 L. Hendriks, A. Gundlach-Graham, B. Hattendorf and D. Günther, Characterization of a new ICP-TOFMS instrument with continuous and discrete introduction of solutions, *J. Anal. At. Spectrom.*, 2017, **32**(3), 548–561.

42 L. Hendriks, V. M. Kissling, T. Buerki-Thurnherr and D. M. Mitrano, Development of single-cell ICP-TOFMS to measure nanoplastics association with human cells, *Environ. Sci.: Nano*, 2023, **10**(12), 3439–3449.

43 P. Menero-Valdes, M. I. Chronakis, B. Fernandez, C. D. Quarles Jr, H. Gonzalez-Iglesias, B. Meermann and R. Pereiro, Single Cell-ICP-ToF-MS for the Multiplexed Determination of Proteins: Evaluation of the Cellular Stress Response, *Anal. Chem.*, 2023, **95**(35), 13322–13329.

44 G. D. Bland, M. Battifarano, A. E. Pradas Del Real, G. Sarret and G. V. Lowry, Distinguishing Engineered TiO(2) Nanomaterials from Natural Ti Nanomaterials in Soil Using spICP-TOFMS and Machine Learning, *Environ. Sci. Technol.*, 2022, **56**(5), 2990–3001.

45 H. Karkee and A. Gundlach-Graham, Characterization and Quantification of Natural and Anthropogenic Titanium-Containing Particles Using Single-Particle ICP-TOFMS, *Environ. Sci. Technol.*, 2023, **57**(37), 14058–14070.

46 A. Hegetschweiler, O. Borovinskaya, T. Staudt and T. Kraus, Single-Particle Mass Spectrometry of Titanium and Niobium Carbonitride Precipitates in Steels, *Anal. Chem.*, 2019, **91**(1), 943–950.

47 S. Bevers, M. D. Montaño, L. Rybicki, T. Hofmann, F. von der Kammer and J. F. Ranville, Quantification and Characterization of Nanoparticulate Zinc in an Urban Watershed, *Front. Environ. Sci.*, 2020, **8**, 84.

48 A. Praetorius, A. Gundlach-Graham, E. Goldberg, W. Fabienke, J. Navratilova, A. Gondikas, R. Kaegi, D. Günther, T. Hofmann and F. von der Kammer, Single-particle multi-element fingerprinting (spMEF) using inductively-coupled plasma time-of-flight mass spectrometry (ICP-TOFMS) to identify engineered nanoparticles against the elevated natural background in soils, *Environ. Sci.: Nano*, 2017, **4**(2), 307–314.

49 S. E. Szakas, R. Lancaster, R. Kaegi and A. Gundlach-Graham, Quantification and classification of engineered, incidental, and natural cerium-containing particles by spICP-TOFMS, *Environ. Sci.: Nano*, 2022, **9**(5), 1627–1638.

50 R. L. Buckman and A. Gundlach-Graham, Machine learning analysis to classify nanoparticles from noisy spICP-TOFMS data, *J. Anal. At. Spectrom.*, 2023, **38**(6), 1244–1252.

51 T. R. Holbrook, D. Gallot-Duval, T. Reemtsma and S. Wagner, Machine learning: our future spotlight into single-particle ICP-ToF-MS analysis, *J. Anal. At. Spectrom.*, 2021, **36**(12), 2684–2694.

52 K. Mehrabi, D. Günther and A. Gundlach-Graham, Single-particle ICP-TOFMS with online microdroplet calibration for the simultaneous quantification of diverse nanoparticles in complex matrices, *Environ. Sci.: Nano*, 2019, **6**(11), 3349–3358.

53 K. Mehrabi, R. Kaegi, D. Günther and A. Gundlach-Graham, Emerging investigator series: automated single-nanoparticle quantification and classification: a holistic study of particles into and out of wastewater treatment plants in Switzerland, *Environ. Sci.: Nano*, 2021, **8**(5), 1211–1225.

1558 | *J. Anal. At. Spectrom.*, 2024, **39**, 1551–1559

This journal is © The Royal Society of Chemistry 2024

54 F. Loosli, J. Wang, S. Rothenberg, M. Bizimis, C. Winkler, O. Borovinskaya, L. Flamigni and M. Baalousha, Sewage spills are a major source of titanium dioxide engineered (nano)-particle release into the environment, *Environ. Sci.: Nano*, 2019, **6**(3), 763–777.

55 H. E. Pace, N. J. Rogers, C. Jarolimek, V. A. Coleman, C. P. Higgins and J. F. Ranville, Determining transport efficiency for the purpose of counting and sizing nanoparticles via single particle inductively coupled plasma mass spectrometry, *Anal. Chem.*, 2011, **83**(24), 9361–9369.

56 A. Gundlach-Graham, S. Harycki, S. E. Szakas, T. L. Taylor, H. Karkee, R. L. Buckman, S. Mukta, R. Hu and W. Lee, Introducing "time-of-flight single particle investigator" (TOF-SPI): a tool for quantitative spICP-TOFMS data analysis, *J. Anal. At. Spectrom.*, 2024, **39**, 704–711.

57 A. Gundlach-Graham and K. Mehrabi, Monodisperse microdroplets: a tool that advances single-particle ICP-MS measurements, *J. Anal. At. Spectrom.*, 2020, **35**(9), 1727–1739.

58 A. Gundlach-Graham, L. Hendriks, K. Mehrabi and D. Gunther, Monte Carlo Simulation of Low-Count Signals in Time-of-Flight Mass Spectrometry and Its Application to Single-Particle Detection, *Anal. Chem.*, 2018, **90**(20), 11847–11855.

59 A. Gundlach-Graham and R. Lancaster, Mass-Dependent Critical Value Expressions for Particle Finding in Single-Particle ICP-TOFMS, *Anal. Chem.*, 2023, **95**(13), 5618–5626.

60 X. Wang, W. Griffin and J. Chen, Hf contents and Zr/Hf ratios in granitic zircons, *Geochem. J.*, 2010, **44**(1), 65–72.

61 F. Gottschalk, T. Sonderer, R. W. Scholz and B. Nowack, Modeled environmental concentrations of engineered nanomaterials (TiO2, ZnO, Ag, CNT, fullerenes) for different regions, *Environ. Sci. Technol.*, 2009, **43**(24), 9216–9222.

This journal is © The Royal Society of Chemistry 2024

J. Anal. At. Spectrom., 2024, **39**, 1551–1559 | 1559